Structural insights into interactions of new polymeric (μ-oxo) bridged Cu(II) complexes of taurine with yeast tRNA by spectroscopic and computational approaches and its application towards chemoresistant cancer lines

Siffeen Zehra, H Khan, Thierry Roisnel, Sartaj Tabassum, Farukh Arjmand

Structural Insights into interactions of new Polymeric (μ–oxo) bridged Cu(II) complexes of Taurine with yeast tRNA by spectroscopic and computational approaches and its application towards chemoresistant cancer lines

Siffeen Zehra[a], Huzaifa Yasir Khan[a], Thierry Roisnel[b], Sartaj Tabassum[a], Farukh Arjmand[a*]

[a]*Department of Chemistry Aligarh Muslim University, Aligarh, U.P, India-202002*

[b]*Institut des Sciences Chimiques de Rennes, UMR 6226, Université de Rennes 1, Campus de Beaulieu Batiment 10B, Bureau, 15335042 Rennes, France*

**Email: farukh.arjmand18@gmail.com*

Abstract

RNA-targeted drugs are considered as safe treatment option for the cure of many chronic diseases preventing off-targeted delivery and acute toxic manifestations. FDA has approved many such RNA therapies in different phases of clinical trials, validating their use for the treatment of various chronic diseases. We report herein, new water-soluble (μ–oxo) bridged polymeric Cu(II) complexes of taurine (2–aminoethane sulfonic acid) complexes **1** and **2**. The therapeutic potency of **1** and **2** was ascertained by studying biophysical interactions with tRNA/ct-DNA. The experimental results demonstrated that the complexes interacted avidly to nucleic acids through intercalation mode depicting a specific preference for tRNA in comparison to ct–DNA and, moreover **2** showed higher binding propensity than **1**. The electrophoretic behavior of the complexes with plasmid pBR322 DNA and tRNA were examined by gel mobility assay that revealed a concentration-dependent activity with complex **2** performing more efficient cleavage as compared to complex **1**. Cytotoxicity results on cancer cell strains displayed higher cytotoxicity than complex **1** against treated cancer cells. The synthesized copper(II) taurine complexes have met the basic criteria of anticancer drug design as they are structurally well-characterized, exhibiting good solubility in water, lipophilic in nature with superior intercalating propensity towards tRNA and cytotoxic in nature.

Keywords: Binding modes; Cu(II) complexes; Drug-RNA interaction; EtBr displacement; cytotoxicity

1. Introduction

Medicinal chemists globally, are in search of 'robust' efficacious safe chemotherapeutic drugs for cancers that can overcome the existing issues of currently used drugs *viz*., acquired resistance, off-target toxicity and severe side effects [1-4]. Many drug design strategies have emerged over a period of time, as most of the existing anticancer drug regimens have failed at one or other stages of R& D or clinical trials that puts huge economic toll on countries and also wasted considerable span of time [5-8]. Amongst the innovative strategies is the use of RNA-based therapeutics that have recently gained much prominence in drug design for the treatment of chronic diseases such as developmental health issues {metabolic, immunological and neurological}and cancers [9-11]. RNAs fold in myriad secondary structural conformations (Hairpin, bulges, loops pseudo knots, etc.) that provide unique binding pockets for selective and specific recognition of small drug molecules [12,13]. In this context, several intercalative cations, antitumor aminoglycoside antibiotics, amino acids and peptides, inorganic compounds that include Schiff base complex drug formulations derived from many bioactive ligands have been explored and their interaction with the therapeutic targets, DNA and sister cousin, RNAs was vigorously undertaken [14]. Transition metal-based drug entities are unique in geometric shapes [15] and exhibit specific preferential disposition at the biological spaces *in vivo*, interact readily by both covalent as well as non-covalent interactions [16]. As a result, inorganic drug candidates may be able to modify or tune the conformation of RNA binding sites depending on the metal involved or the bioactive ligand scaffolds, and they may do so with exceptionally specific molecular selectivity and recognition [17].

Literature reports reveal that structure-based design motifs are pharmaco-kinetically more drug-likely in terms of drug stability, delivery and specificity towards therapeutic targets at the molecular levels [18]. Nevertheless, one of the important identified hurdles for the failure of drugs is poor solubility in water, which limits the evaluation of their pharmacokinetic parameters from *in vitro* to pre-clinical *in vivo* research [19]. Literature reports reveal that drugs with low water solubility have a low oral bioavailability that show varied clinical response. To address the solubility issue, medicinal chemists have utilized water soluble analogues of such therapeutics [20] obtained by modifying the core ligand framework by incorporating sulfonic functional groups such as taurine ligands. The sulfur-containing analogue of β–amino acid, taurine (2–aminoethane sulfonic acid) is the ubiquitous free amino acid discovered in the mammalian tissues [21]. It is involved in many physiological processes such as cell membrane stabilization, regulating intracellular calcium levels, cell growth and differentiation [22,23]. Taurine and its derivative compounds exhibit remarkable anticancer effects that could be manifested by the following i) suppression of cell proliferation ii) downregulating the angiogenesis process and iii) enhancing the tumor cell apoptosis by scavenging upon the reactive oxygen species [24]. Recent studies have suggested that the intracellular taurine levels could predict the formation of certain tumors and serve as novel biomarkers to diagnose cancers like breast and bladder cancer at an early stage. Therefore, taurine-as a pharmaceutical auxiliary scaffold can be added for better therapeutic response in many classes of anticancer agents [25]. Earlier reports from Schiff bases having taurine moiety exhibit myriad coordination modes while a ternary complex interacts by characteristic aromatic-ring stacking intercalation mode that could stabilize the double-helical structure of therapeutic target, DNA. H. Liang *et al*. reported a Cu(II) complex, [Cu(sal–tau(phen)]1.5H_2O possessing salicylaldehyde–taurine Schiff base and 1,10–Phenanthroline and

studied its DNA interaction behaviour. They demonstrated a dose-dependent antitumor effect on cell cycle and apoptosis in MGC-803 cells [26]. However, there are fewer reports of taurine Schiff base complexes targeted to tRNA that show exceptional anticancer profile. A conjugate is formed by taurine with a uridine residue of $tRNA^{Leu(UUR)}$ in normal mitochondria. The conjugation reaction can improve the interaction of the tRNA's AAU anticodon as the modified uridine residue is situated in the anticodon's wobble location. [27].

Copper complexes have appeared as the most prominent potent class of drugs having anticancer properties [28-30] and a series of copper compounds casiopeínas® have entered phase I clinical trials [31], however, they exhibit very low aqueous solubility. Interestingly, copper complexes exhibit a good cytotoxic response against different cancer cell strains and are capable of inhibiting cancerous cells' growth in a dose-dependent manner at a low micro-molar IC_{50} values [32]. Copper-based anti-cancer agents are known to kill cancer cells by various mechanisms such as generation of reactive oxygen species (ROS), proteasome inhibition, DNA damage via apoptosis etc [33-36].

The combinational cocktail targeted therapy incorporating multiple bioactive ligands in a single entity such as electron-rich heterocyclic imidazole as a co-ligand with Schiff base anchoring fragment is a unique approach that has proved instrumental for imparting enhanced cytotoxic activity with reduced toxicities that may necessitate a reduction in dosage of drugs. Previous literature reports revealed that imidazole-based compounds are proven as potent anti-cancer, anti-inflammatory, and antiviral agents [37,38]. Imidazole is an aromatic moiety having both polar and ionizable property that is known to improve pharmacokinetic properties, enhance the solubility and bioavailability of therapeutic drug candidates [39]. The synthesized polymeric copper(II) taurine Schiff base appended with imidazole ligand **1** and **2** drug entities reported,

herein, are exceptionally unique in design, structurally well characterized, specifically targeted to tRNA, fairly soluble in water and capable of inducing ROS mediated cell death in cancer cells.

2. Experimental

Synthesis of Complexes

To the stirred methanolic solution of 2−Aminoethane sulfonic acid (0.125 g, 1 mmol) was added 2–Hydroxy–3–methoxybenzaldehyde (0.152 g, 1 mmol)/ 3–Hydroxy–2–naphthaldehyde (0.172 g, 1 mmol) and the reaction mixture was kept on reflux for 3 h to yield a yellow-colored solution. The completion of the reaction was monitored by using TLC and subsequently $Cu(CH_3COO_2).H_2O$ (0.199g, 1 mmol) was added which resulted in green colored solution. After half an hour a methanolic solution of imidazole (0.068 g, 1 mmol) was added to the reaction. The reaction mixture was filtered and kept aside at room temperature. Suitable green, thin, needle like crystals were obtained from mother liquor after 3–4 days.

Complex $[C_{13}H_{15}CuN_3O_5S]$, **1**: Yield: 85%, M.P: 235˚C, Anal. (%) Calc. for $C_{13}H_{15}CuN_3O_5S$: C (41.73), H (4.25), N (10.43), Found: C (41.74), H (4.24), N (10.45). FT−IR (KBr cm^{-1}): 1622 ν(HC=N), 1243, 1139 ν(S=O), 1474 ν(C=N) imidazole, 543 ν(M−O), 486 ν(M−N). UV−vis (λ_{max}, nm) in DMSO: 263 (π −π*), 347 (n−π*), 678 (d−d). ESI−MS (m/z): 387 $[C_{13}H_{14}CuN_3O_5S]^+$.

Complex $[C_{16}H_{15}CuN_3O_4S]$, **2**: Yield: 87%, M.P: 248˚C, Anal. (%) Calc. for $C_{16}H_{15}CuN_3O_4S$: C (46.88), H (3.93), N (10. .43), Found: C (41.74), H (4.24), N (10.45). FT−IR (KBr cm^{-1}): 1618 ν(HC=N), 1236, 1136 ν(S=O), 1434 ν(C=N)imidazole, 588 ν(M−O), 499 ν(M−N). UV−vis (λ_{max}, nm) in DMSO: 266 (π −π*), 354 (n−π*), 680 (d−d). ESI−MS (m/z): 403 $[C_{16}H_{14}CuN_3OS−3H]+$.

3. Results and discussion

Two polymeric imidazole appended water-soluble Cu(II) complexes **1** and **2** have been prepared as shown in Scheme **1.** Light green, thin, needle-like transparent crystal of complex **1** was obtained from the mother liquor, while in the case of complex **2**, the compound was crystallized

in a solvent system containing methanol and water (1:1). The spectroscopic techniques (FT-IR, UV–vis and EPR), ESI–MS as well as single X-ray crystallographic studies were utilized to establish the molecular structure of complexes **1** and **2**. The complexes were discovered to be air-stable and found to be soluble in water, MeOH, EtOH, Dimethylsulfoxide (DMSO) as well as Dimethylformamide (DMF).

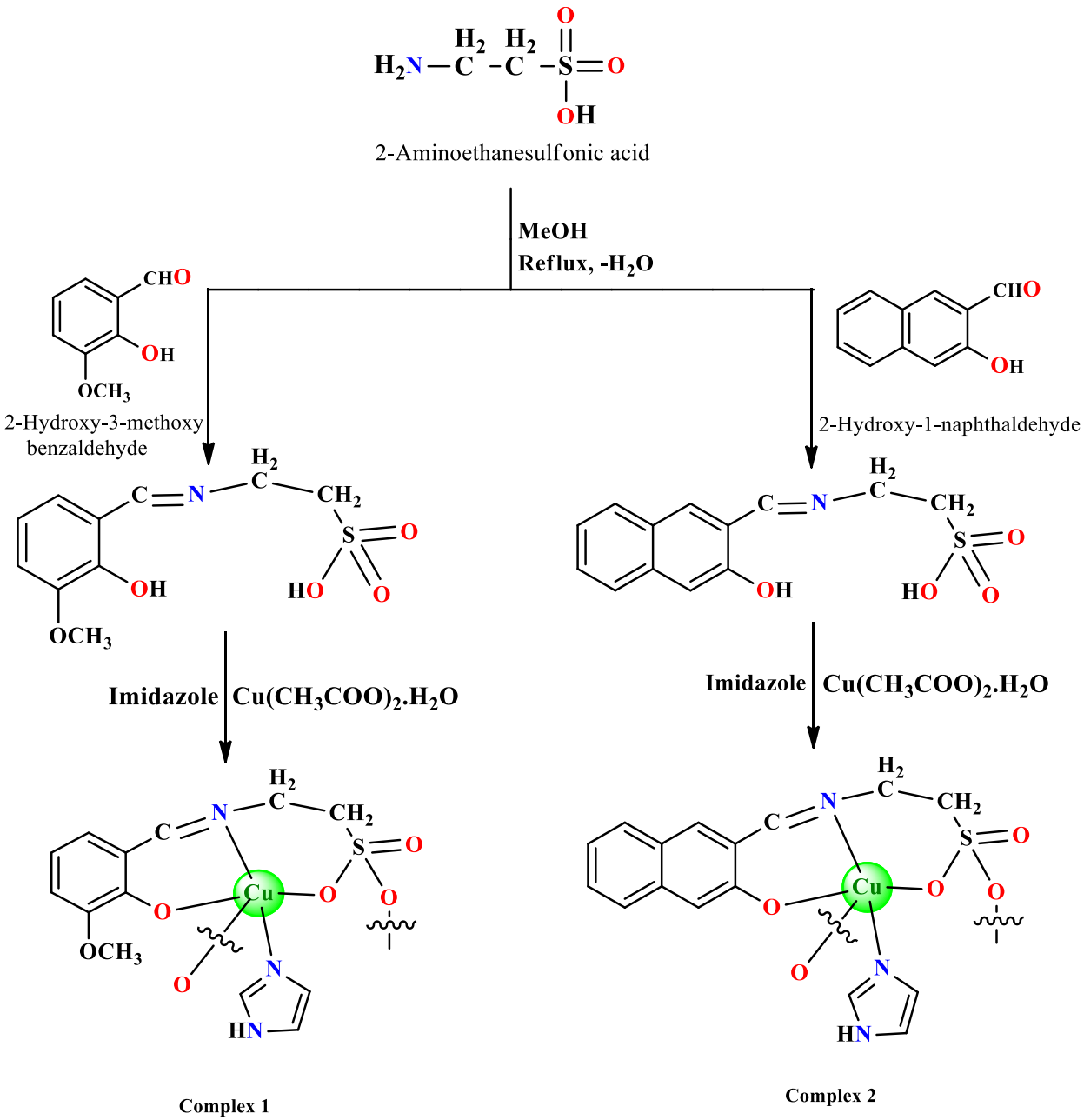

Scheme 1. Synthetic route to prepare the complexes **1** and **2**.

Spectroscopic characterization

3.1 IR Spectral studies

The complexes **1** and **2** showed the presence of vibration bands associated to ν(–C=N) stretching of the azomethine group centered at 1622 and 1618 cm^{-1}. The characteristic vibrational frequencies for the stretching modes of υ(S=O) group were observed at 1243 and 1139 cm^{-1} for **1** while at 1236 and 1136 cm^{-1} for **2** [40]. The absorption bands for the ν (C–N) stretching vibrations corresponding to an imidazole ligand were observed in the range of 1474-1434 cm^{-1}. Far-IR spectra of complexes **1** and **2** exhibited peaks in the range of 588−543 cm^{-1} and 499−486 cm^{-1} attributed to ν(Cu−N) and ν(Cu−O) stretching vibrations, respectively.

3.2 Electronic Spectral studies

The absorption spectra of **1** and **2** were recorded in conc. range 200−700 nm in methanol. The UV-vis spectrum showed bands at 263 and 266 nm in the UV region that were attributed to electronic transitions (π–π*) of the aromatic chromophore while LMCT bands (ligand-to-metal charge transfer) appeared at 347 and 354 nm. These complexes **1** and **2** also displayed lower energy d−d bands due to the $^{2}Eg \rightarrow {}^{2}T_{2g}$ transition centered at 678 and 680 nm in the visible region. The electronic spectral data indicated that the complexes formed distorted square pyramidal geometry around Cu(II) well-corroborated with single X-ray crystal diffraction studies [41].

3.3 EPR Spectral studies

The EPR spectra of complexes **1** and **2** in the polycrystalline form were acquired at room temperature (Fig. S1) to investigate the coordination geometry of the complexes. Complex **1** showed a single broad signal with g∥ at 2.34 and g⊥ at 1.92, whereas complex **2** had g∥ signals at 2.28 and g⊥ at 1.90, which implicated a penta-coordinated geometry around the Cu(II) metal

centers. The penta coordinated complexes with g∥ value greater than g⊥ suggested a distorted square pyramidal environment, ruling out the behaviour of complexes possessing a trigonal bipyramidal geometry [42].

3.4 Mass Spectral studies

The ESI–MS spectra of complexes **1** and **2** were recorded, which shows positive ion peaks [M^+] at *m/z* values corresponding to the molecular formulas of the complexes (Figure S2). The complex **1** showed a molecular ion peak at *m/z* = 387 corresponding to the $[C_{13}H_{14}CuN_3O_5S]^+$ and an isotopic peak at *m/z* = 389. Another peak was observed due to the removal of imidazole ligand moiety at *m/z* = 319 attributed to the molecular fragment $[C_{10}H_{10}CuNO_5S]^+$ along with an isotopic peak at *m/z* = 320. Complex **2** revealed a peak at *m/z* = 403 corresponding to the fragment $[C_{16}H_{14}CuN_3O_4S–3H^+]$ and other peak at *m/z* = 340 due to removal of imidazole ligand with $[C_{13}H_{10}CuNO_4S+2H^+]$. Complexes **1** and **2** also showed peaks at *m/z* = 257 and 278, which are assignable to the ligand moieties with molecular fragments $[C_{10}H_{12}NO_5S–H]^+$ and $[C_{13}H_{12}NO_4S]^+$. Thus, the mass spectra of complexes **1** and **2** correlated well with their predicted molecular structures.

3.5 Single X-ray crystal structure description

The complex **1** crystallizes in the trigonal crystal system with the R–3 space group, according to single X-ray crystal diffraction experiments. The copper metal center adopted a distorted pentacoordinated square pyramidal geometry via coordinating through the N_2O_3 donor set. The coordination sphere consists of –ONO donor set from the tridentate Schiff base ligand, one nitrogen atom from the imidazole and one oxygen atom from the sulfonate group of the neighboring imine ligand occupying the axial position and acting as a “bridge” between the two copper centers arranged perpendicularly (Fig. 1). The oxygen atom at the apex of the pyramid possesses a longer Cu–O bond distance (2.506 Å) than Cu–O bonds (1.907–2.001Å) in the basal

plane, demonstrating the presence of Jahn–Teller distortion. The elongation results from the unsymmetrical occupation of the electrons present in the d–orbital of the Cu(II) atom, where two electrons are found in the d_z^2 while one electron is accommodated in the $d_{x^2-y^2}$ orbital. The deviation from the equatorial plane in complex **1** was also ascertained by measuring the trans angles, i.e., N(1)–Cu(1)–O(19) and N(11)–Cu(1)–O(31), which were found to be 88.33º and 94.02º, respectively. The trigonality index (τ) value was calculated according to Addison–Reedjik geometric parameter i.e., $\tau = (\beta-\alpha)/60$ where α and β represents the two largest angles around the copper center. The value of trigonality index for ideal square pyramidal geometry is zero and for perfect trigonal bipyramidal $\tau = 1$. In our case, at the Cu(II) site it was found to be $\tau = 0.069$, close to the index expected for a distorted square pyramidal geometry. The two Cu(II) metal centers are 5.10 Å distance apart from one another.

Significant intermolecular hydrogen and C---C bonding interactions were also present along the c axis in a one-dimensional polymeric array of the crystal (Fig. 2). Complex **1** showed extensive hydrogen bonding between the hydrogen atoms of imidazole and oxygen atom of the Schiff base ligand and C---C bonding interactions between the C5 carbon atoms of imidazole rings arranged in an antiparallel fashion generating a one dimensional (1D) polymeric array along the c axis.

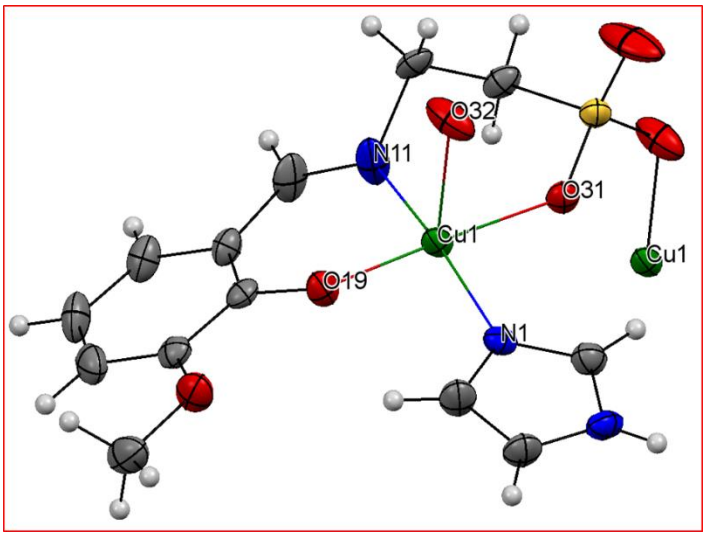

Fig. 1. The crystal structure of complex **1** drawn at 50% probability level.

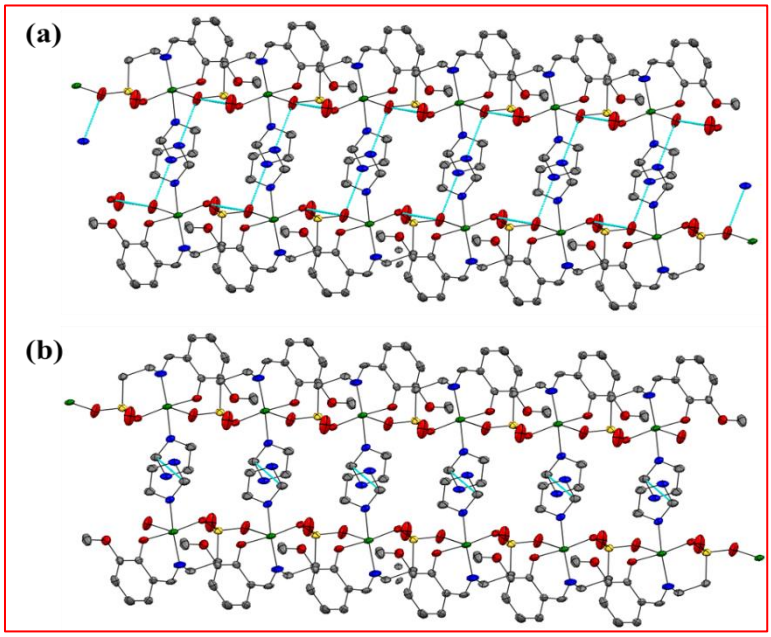

Fig. 2. 1D polymeric structure in complex **1** showing intermolecular (a) hydrogen and (b) carbon-carbon bonding interactions along the *c* axis.

The crystallographic details of complex **2** revealed that the complex crystallizes in a monoclinic crystal system with the $P2_1/n$ space group. The copper(II) metal ion acquired a five coordinated distorted square pyramidal geometry at the center by coordinating *via* N_2O_3 donor set. The coordination sphere consists of a tridentate Schiff base ligand providing the –ONO donor set, one imidazole ligand offering the nitrogen atom, and one oxygen atom from the sulfonate group of the adjacent imine ligand, which occupies the apical "bridging" position between the two copper centers (Fig. 3).

The axial position was occupied by oxygen atom of the pentacoordinated copper center revealed an elongated Cu(1)–O(12) bond (2.643 Å) as compared to the Cu–O bonds (1.909–1.993 Å) present in the basal plane. The lengthening of the bonds was attributed to the unequal/asymmetrical distribution of the d-electrons resulting in Jahn-Teller distortion within the crystal system. The trans angles in complex **2** showed deviation from the planarity, which were found to be N(16A)–Cu(1)–O(11) = 92.90° and N(1)–Cu(1)–O(28) = 88.70°, respectively. The

trigonality index was found to be τ = 0.075, which is close to the value for ideal square pyramidal geometry, i.e., τ = 0. The distance between the two Cu(II) centers that are arranged perpendicular to each other was found to be 5.24Å.

The crystal structure of complex **2** involves significant intermolecular hydrogen bonding interactions between the hydrogen atoms of imidazole (H3) and an oxygen atom (O12) of the Schiff base ligand where the imidazole rings are arranged in an antiparallel manner providing a ladder-like conformation to the polymer (Fig. 4). The structure of complex **2** was further stabilized by the presence of intermolecular C---C bonding interactions between the C2 carbon atoms of the imidazole ring and stacking interactions among the phenyl rings of the Naphthaldehyde group generating a 2D polymeric array along the *c* axis.

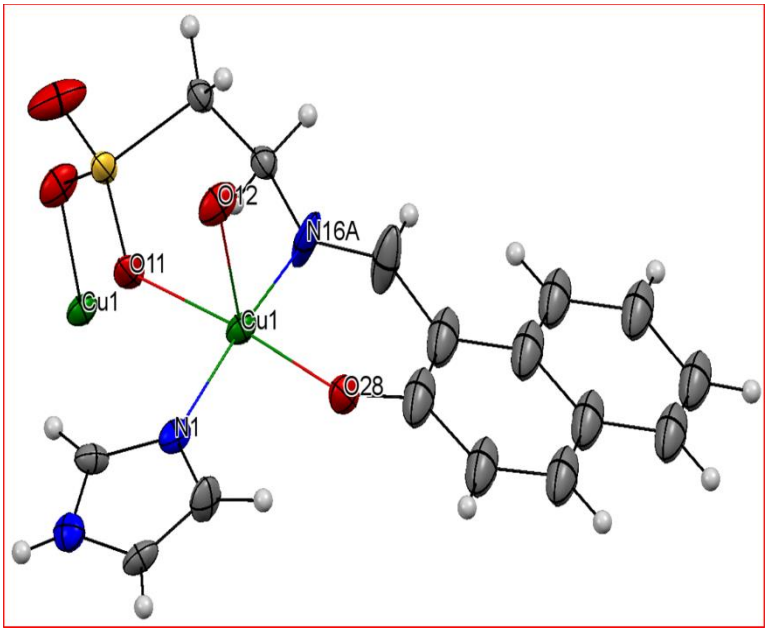

Fig. 3. ORTEP view for the crystal structure of complex **2** drawn at 50% probability level.

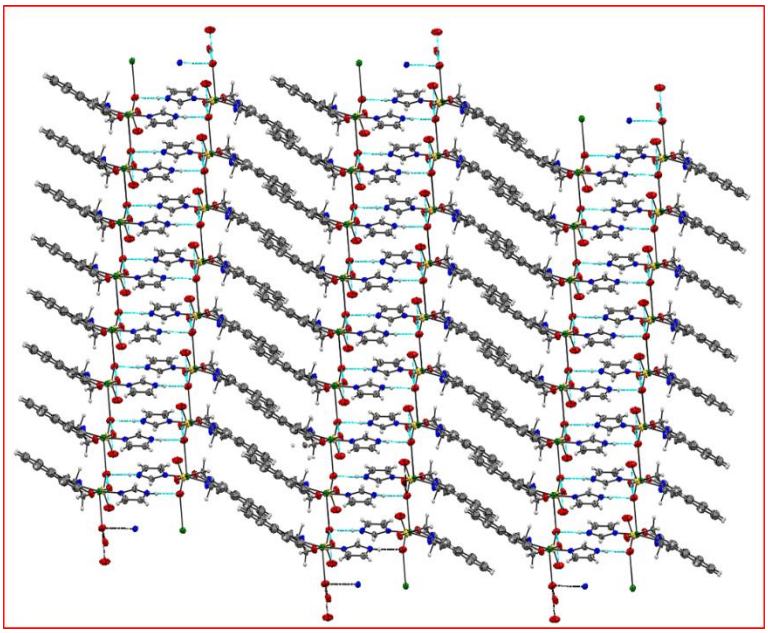

Fig. 4. 2D ladder-like polymeric array in complex **2** revealing intermolecular hydrogen bonding interactions along the *c* axis.

3.6 Density functional theory computational studies

Density Functional Theory (DFT) computational studies were used to optimize the electronic structure and calculate various geometrical parameters of **1** and **2** using ORCA 3.0.1 program suite. The initial geometries which were subjected to optimization were taken from the X-ray crystallographic data of complexes **1** and **2** (Fig. S3). The associated geometrical parameters, including bond angles as well as bond lengths are determined from the optimized structures and were found to correlate with the crystallographic data as presented in Tables S4 and S5. However, slight differences in the values resulted from the optimization studies in the gas phase, whereas the experimental data were collected in the solid phase.

The frontier molecular orbitals of a complex were related to optical and absorption properties, and the HOMO and LUMO energy gap was associated with the kinetic stability and chemical reactivity. The analysis of FMOs of **1** and **2** demonstrated that the LUMOs mainly outspread over the amine nitrogen and the aromatic ring of the Schiff base ligand while the HOMOs were dispersed around the metal coordinated sulfonate group of the Schiff base and the imidazole

ligand. The LUMOs are responsible for the electron-donating ability of the coordinated ligand in the unoccupied metal-centered orbitals, whereas the HOMOs show the electron-accepting ability within the delocalized orbitals (Fig. 5). The energy for the LUMO and HOMO orbitals were observed in negative values, which demonstrated that the complexes are thermodynamically stable in nature. Further, the orbital analysis for complexes **1** and **2** shows that the E_{LUMO} values were –1.770 and –2.121 eV, whereas E_{HOMO} values were found to be –5.568 and –5.961 eV, respectively. The ΔE values resulted from the DFT calculations were found as –3.798 eV and –3.840 eV for **1** and **2**. These values determined that complex **2** had a higher stability in comparison to **1**. In conclusion, higher stability of complex **2** and the lower energy band gap values compared to **1** were observed in concordance with the findings observed from various *in vitro* assays.

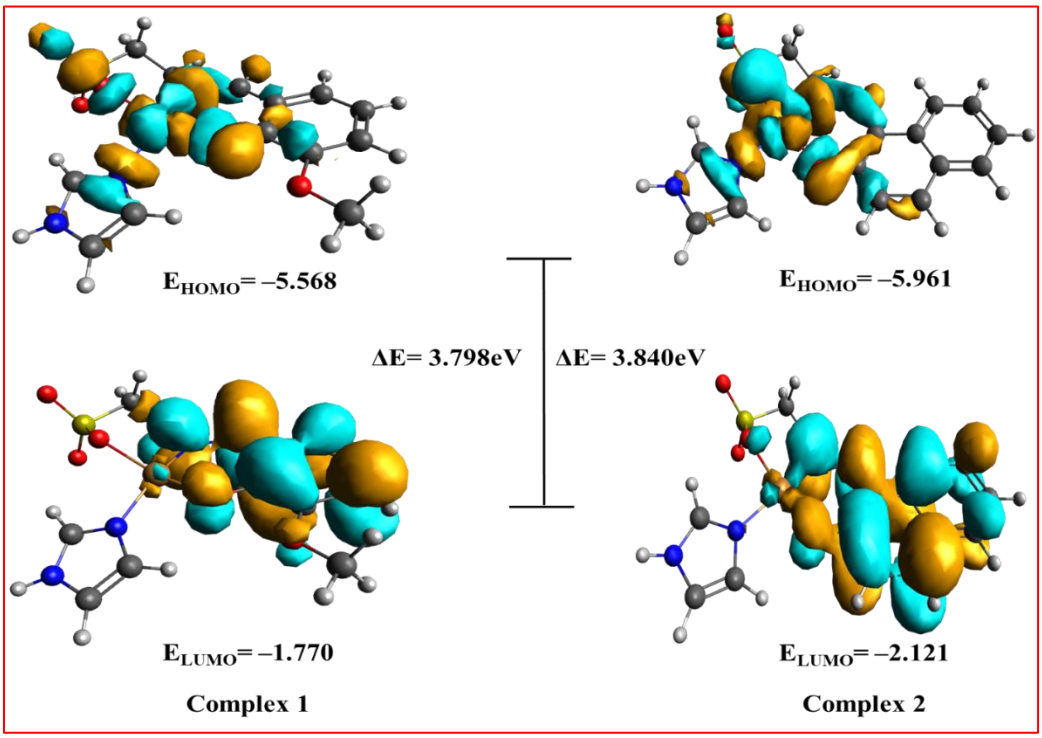

Fig. 5. Frontier molecular orbitals contour plot of **1** and **2**.

3.7 Hirshfeld surface analysis

The Hirshfeld surface analysis was performed for complexes **1** and **2** as shown in Fig. S4, mapped over d_{norm}, shape index, and curvedness. The d_{norm} surface displayed circular red color depressions which arise from the O----H interactions within both the complexes. The shape index surface demonstrated the red and blue conjoined triangles in the shape of "bow–tie" patterns which were attributed to shape the π–π stacking interactions in the crystal structures of the complexes [43].

The two-dimensional fingerprint plots were generated to make it easy to quantify distinct intermolecular interactions coming from different atomic pairs [44]. As shown in Fig. S5, two sharp spike-like structures were observed around the lower left of the plots, which were typical of O----H/ H----O interactions and comprised 21.9% and 25.1% of the total Hirshfeld surfaces of **1** and **2**, respectively. The H----H interatomic contacts which were discovered to be another dominating interactions contributing 45.2% and 31.2% to the total surface contribution in **1** and **2**. The fingerprint plots also show the characteristic "wing" like structures that arise from C----H/ H----C interactions and contribute 17.7% in complex **1** and 30.2% in complex **2** of the total surface area.

3.8 Stability studies in solution

The stabilities of the complexes have been confirmed by absorption spectroscopic technique. The absorption spectra of both the complexes were performed in DMSO as well as in water at distinct time intervals of 0 h, 1 h, 12 h and 24 h. The results showed that neither the intensity nor the position of the absorption bands had significantly changed. Furthermore, even after 24 hours, no discernible changes in the absorption spectra were seen, demonstrating the stability of their geometries and coordinating spheres. (Fig. 6, S9)

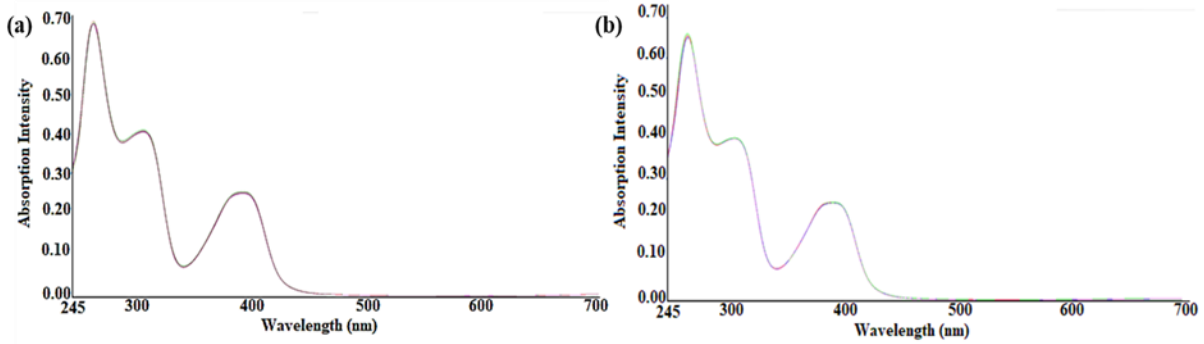

Fig. 6. Stability studies of complexes **1 (a)** and **2 (b)** in DMSO at different time intervals (0h, 1h, 12h, 24 h), [Complex **1**] = [Complex **2**] = 10^{-3} M

3.9 Binding profile with therapeutic targets, ct–DNA/tRNA

In vitro interactions with complexes **1** and **2** were performed to investigate their binding mode, and their preferential selectivity towards ct–DNA and RNA as therapeutic targets. Since most of the prominent metal-based anticancer drugs in clinical use have their pharmacological target as DNA, targeting DNA provides a rationale therapeutic approach for their drug design. In the recent past, RNAs have gained paramount importance for designing efficient metal-based drug candidates due to their biological role and diverse structural motifs providing unique binding pockets for selective specific recognition. Despite this, there are fewer reports that describe the binding profile of small metal-based drug candidates such as Schiff base complexes with tRNA. Thus, investigating the molecular mechanism of metallo-drugs targeted to tRNA biomolecule serves as a prerequisite to design efficient metal-based chemotherapeutic agents.

3.9.1 Absorption spectral studies

To determine the binding propensity and target selectivity of complexes **1** and **2**, absorption titration experiments with ct–DNA and tRNA were performed. Titration curves of complex 1 with increasing ct–DNA/tRNA concentration in aqueous Tris-saline buffer revealed an increase in the absorption spectrum at the ligand centered π–π* (λ = 277) and while a decrease at the

LMCT band (λ = 396) along with a redshift (6–7 nm) (Fig. 7) were observed. Such spectral changes implicate a partial intercalative binding mode of the complex **1** [45]. On the other hand, complex **2** exhibited a decrease in in the absorption intensity at π–π* (λ = 304) band and at the LMCT band (λ = 403 nm). The "hypochromic effect" in absorption spectra of complex **2** could be ascribed to π–π stacking interactions between the planar aromatic chromophore of Schiff base ligand scaffold and nucleobases of ct–DNA and tRNA molecules, which is compatible with an intercalative binding mode [46].

Complex **1** suggested 15.43% and 17.85% hypochromism, whereas complex **2** resulted in 19.04% and 21.41% hypochromism for ct–DNA and tRNA, respectively. The greater extent of hypochromism towards the biomolecules for **2** resulted in higher binding affinity in comparison to **1**. To further quantify the extent of binding, Wolfe-Shimer equation [47] was used to calculate K_b values, and the values are presented in Table 1. The values for Gibb's free energy were also evaluated for **1** and **2**. Furthermore, higher values of K_b upon interaction with tRNA clearly indicate the preferential selective binding of the complexes towards RNA as compared to ct–DNA.

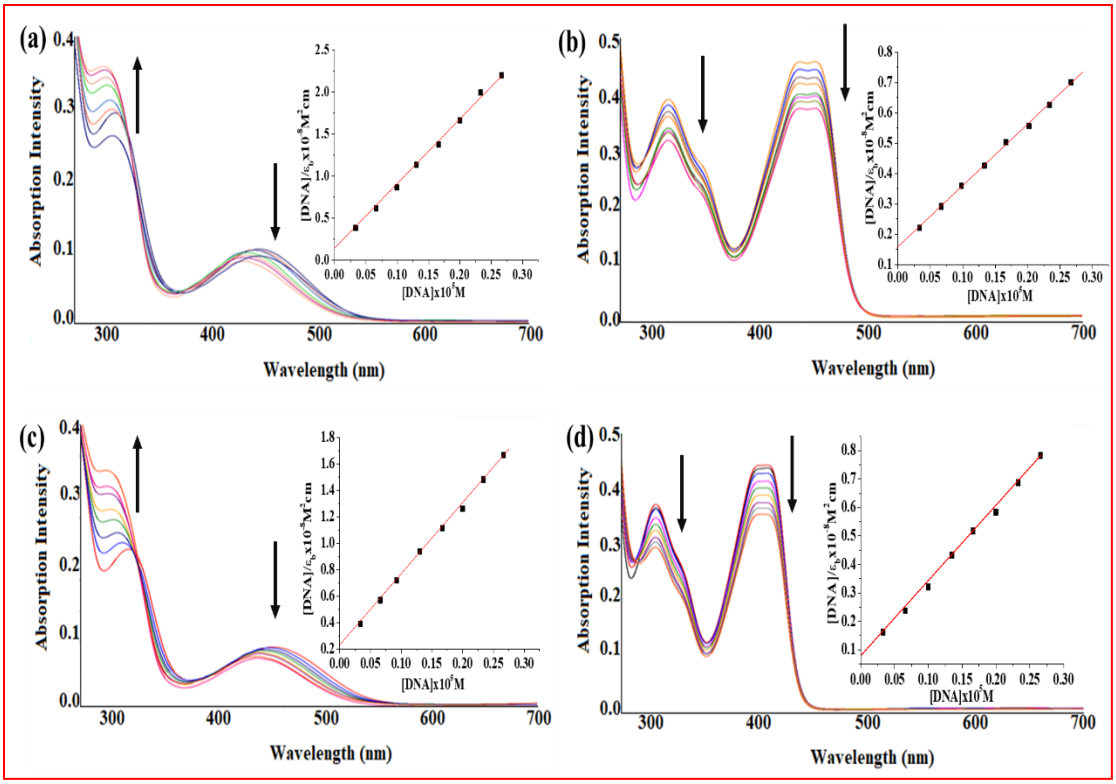

Fig. 7. Changes in absorption intensity of complexes **1** and **2** with progressive addition of DNA (a and b) and tRNA (c and d), respectively.

3.9.2 Fluorescent intercalator displacement assays

To gain a better understanding of the mode of interaction, a fluorescent intercalator displacement assay with increasing aliquots of **1** and **2** using ethidium bromide was carried out. With the subsequent addition of **1** and **2** (Fig. S6), the emission intensity decreased as the bound intercalator, ethidium bromide was gradually replaced from the ct–DNA/tRNA nucleobases. The observed shifts in the emission intensity of **1** and **2** suggested an intercalative binding mode towards ct–DNA and tRNA [48]. The classical Stern–Volmer equation was applied to calculate the quenching constant Ksv values (Fig. 8) for complexes **1** and **2**. The complex **2** observed higher K_{sv} value, as shown in Table 1, which revealed its stronger quenching ability than complex **1** towards ct–DNA/tRNA biomolecule.

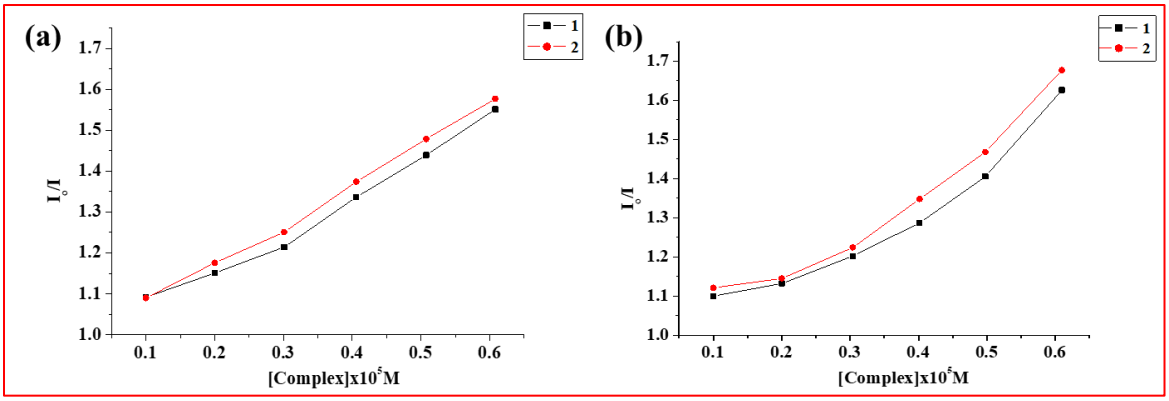

Fig. 8. K_{sv} plots of complexes **1** and **2** towards binding with (a) ct–DNA and (b) tRNA..

Table 1. Binding values of complexes **1** and **2** on the interaction with ct–DNA and tRNA.

Complexes	K_b (M^{-1})		ΔG (KJ/mol)		% Hypo chromism		K_{sv} (10^5 M^{-1})	
	DNA	RNA	DNA	RNA	DNA	RNA	DNA	RNA
1	4.37(±0.04) x10^5	5.62(±0.02) x10^5	–32.15	–32.77	15.43	17.85	1.07	1.37
2	5.82(±0.05) x10^5	6.34(±0.03) x10^5	–32.87	–33.07	19.04	21.41	1.15	2.21

3.9.3 Circular dichroic studies

Circular dichroic spectral studies were carried out to analyze the conformational alterations in the secondary structure of ct–DNA and tRNA macromolecules. The CD spectrum of the B–form ct–DNA exhibited a positive peak centered at 275 nm arising from nucleobase stacking and a negative peak at 245 nm due to helicity. Intercalative binding resulted in significant perturbations of these optical signatures; however, electrostatic interactions or groove binding causes less or no disruption in these bands.

Upon addition of **1** and **2**, there is an upward shift in the positive signal and a decrease in the negative signal along with a wavelength shift in the ct–DNA's CD spectrum was observed, as shown in Fig. 9. Such changes were suggestive of the intercalative mode of binding of the complexes within the DNA helix, causing unwinding and inducing conformational changes in the B–DNA structure [49].

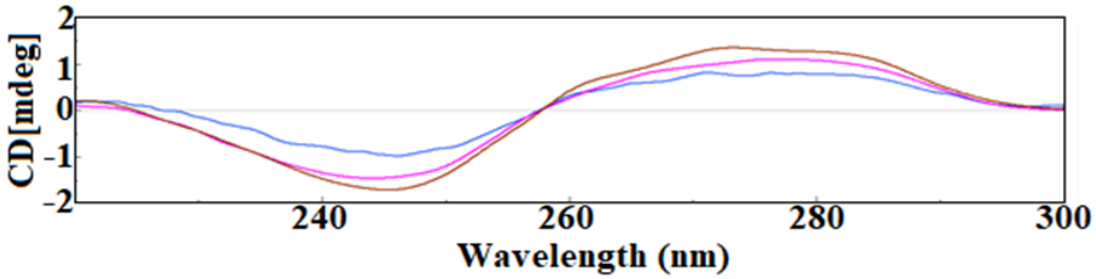

Fig. 9. CD spectra of ct–DNA alone (blue) and in the presence of complexes **1** (pink) and **2** (brown).

Due to ellipticity, the CD spectrum of tRNA revealed two positive bands at 270 and 221 nm, while the right-handed helical A–conformation showed two negative peaks at 240 and 208 nm. Upon incubation of **1** and **2**, a marked increase was observed in the positive bands and a decrease in the signal intensity of the negative bands accompanied by a wavelength shift (Fig. 10). These spectral changes suggested that the complexes interact *via* intercalative mode resulting in conformational changes within the tRNA molecule [50].

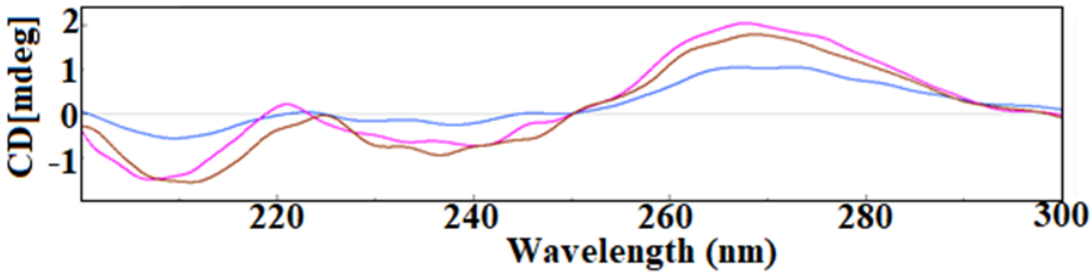

Fig. 10. The observed shifts in CD spectra of tRNA molecule upon interaction with complexes **1** (pink) and **2** (brown). Spectrum of tRNA alone was indicated with blue line.

3.9.4 EPR interaction studies

Previous literature reports have shown that the copper(II) ion could attack the DNA base pairs and coordinate monodentately with the ring nitrogen atom of the guanine nucleobases at pH=7.5 [51]. With the addition of nucleic acids, EPR signal intensity either diminutes or increases, which suggested interaction of metal complexes with the ct–DNA/tRNA. EPR spectral measurements were performed to investigate the binding of Cu(II) complexes with ct─DNA/tRNA. The low-temperature X–band EPR spectrum of **1** and **2** with ct–DNA and tRNA

at physiological pH are presented in Fig. 11. The EPR spectra of **1** and **2** in the frozen solution state revealed a single resonance at g∥ and g⊥, which were characteristic of coupled Cu(II) ion. However, upon addition of an equivalent amount of ct–DNA/ tRNA to **1** and **2,** the spectral signatures revealed a shift in EPR spectral signatures along with the hyperfine splitting having g∥ and g⊥ values corresponding to the copper complex with apical chelation by a donor atom.

The structural features of complexes **1** and **2** show that Cu(II) was coordinated through two nitrogen atoms and two oxygen atoms in the equatorial plane, with one of the oxygen atoms coordinated at the axial site. After titration with ct–DNA /tRNA, EPR spectra suggested that the Cu(II) was bound equatorially with one nitrogen from DNA/RNA base after the replacement of axially coordinated oxygen atom [52]. Furthermore, the signal intensity was diminished to a larger extent with the addition of tRNA, resulted in a stronger interaction of the complexes with tRNA as compared to ct–DNA. The changes observed in the EPR spectral parameters of complexes **1** and **2** in the absence and presence of ct─DNA /tRNA are shown in Table 2.

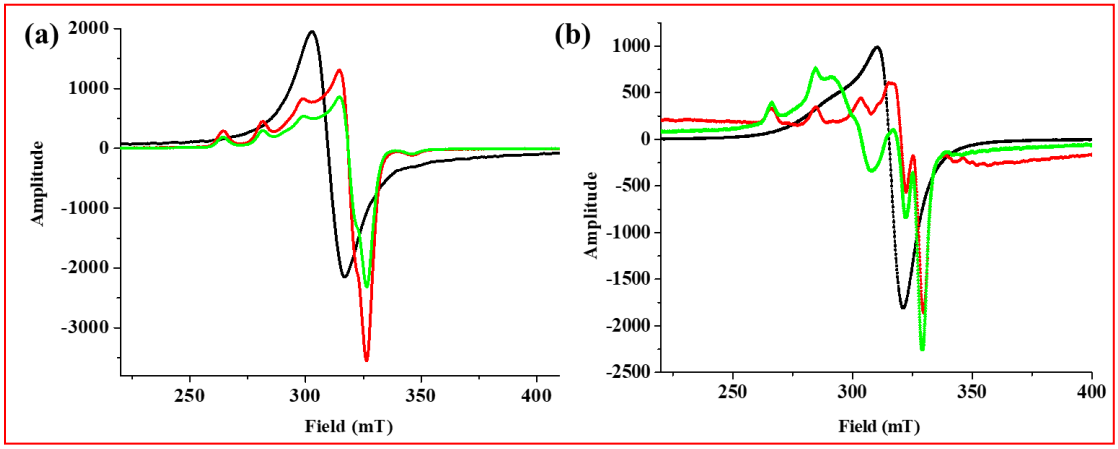

Fig. 11. EPR spectra of **1** and **2** (black) show shifts in the signal amplitude on interaction with ct–DNA (red) and tRNA (green).

Table 2. EPR spectral parameters of complexes **1** and **2**.

Complexes	Complex alone	Complex + ct–DNA	Complex + tRNA
1	$g_{\|}$ =2.34, $g_{\perp}$=1.94	$g_{\|}$ =2.47, $g_{\perp}$=1.88	$g_{\|}$ =2.32, $g_{\perp}$=1.89
2	$g_{\|}$ =2.39, $g_{\perp}$=1.93	$g_{\|}$ =2.45, $g_{\perp}$=1.90	$g_{\|}$ =2.31, $g_{\perp}$=1.88

3.9.5 Cleavage studies pBR322 DNA

The DNA cleavage mechanism plays an important role in cellular biology as it can cause DNA damage, prevent replication, and ultimately results in cell death. [53] Metal complexes could exert their cytotoxic effects by inducing DNA damage through redox activity or hydrolysis of phosphate sugar backbone. Thus, studying the cleavage mechanism provides a pathway for designing efficient metallonucleases which were capable of inducing DNA damage.

Gel electrophoresis is a frequently used technique for evaluating DNA cleavage behaviour by measuring the variations in DNA mobility when an electric field is applied to incubated complexes. When plasmid DNA is subjected to electrophoresis, the fastest travelling supercoiled form (Form I) is converted to a relaxed nicked form (Form II), implying single-strand DNA scission. Between Form I and Form II, on the other hand, the development of the linearized form of DNA (Form III) predicted more lethal double-strand breaks of the DNA helix inducing cell death.

To investigate the DNA cleaving activity of **1** and **2**, a concentration-dependent pBR322 DNA agarose gel electrophoretic assay was performed under physiological conditions. With the progressive addition of complexes **1** and **2**, the plasmid DNA was incubated for 1 h, and the electrophoretic bands showed that the supercoiled form (Form I) was converted to nicked circular form (Form II) along with the appearance of the linearized form (Form III) (Fig. 12 a & b*)*. These results demonstrated that complexes **1** and **2** had the ability to induce double-strand DNA cleavage at low micromolar concentrations. Furthermore, complex **2** was able to induce

much more efficient cleavage at 5 μM as compared to complex **1** whose cleavage activity was observed at 8 μM.

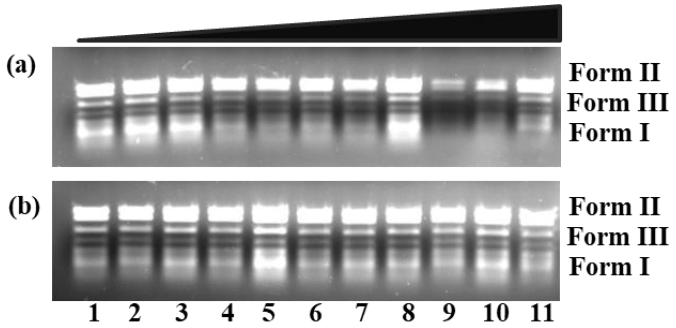

Fig. 12. Complexes **1** and **2** showed pBR322 DNA cleavage (0.1 μg/μL) at different concentrations at 37 °C with an incubation time of 1 h: (a) lane 1, DNA; lane 2, DNA + **1** (1μM); lane 3, DNA + **1** (2μM); lane 4, DNA + **1** (3μM); lane 5, DNA + **1** (4μM); lane 6, DNA + **1** (5μM); lane 7, DNA + **1** (6μM); lane 8, DNA + **1** (7μM); lane 9, DNA + **1** (8μM); lane 10, DNA + **1** (9μM); lane 11, DNA + **1** (10μM); lane 12, DNA + **1** (11μM); (b) lane 1, DNA; lane 2, DNA + **2** (1μM); lane 3, DNA + **2** (2μM); lane 4, DNA + **2** (3μM); lane 5, DNA + **2** (4μM); lane 6, DNA + **2** (5μM); lane 7, DNA + **2** (6μM); lane 8, DNA + **2** (7μM); lane 9, DNA + **2** (8μM); lane 10, DNA + **2** (9μM); lane 11, DNA + **2** (10μM); lane 12, DNA + **2** (11μM).

Earlier reports observed that the copper(II) complexes had the ablilty to cleave the plasmid DNA in H_2O_2 presence via an oxidative pathway mediated through Fenton's mechanism. In lieu of this, the cleavage behaviour of **1** and **2** was studied with the addition of H_2O_2 as a redox agent. The gel electrophoretic bands (Figure 12 a & b, lane 3) demonstrated that the complexes were found to effectively cleave the DNA with the addition of H_2O_2, suggesting the involvement of hydroxyl radicals in the cleavage pathway following an oxidative mechanism.

To explore the role of various reactive oxygen species in the cleavage mechanism, the complexes were incubated with different additives such as singlet oxygen quencher (NaN_3), superoxide oxygen scavenger (SOD), and hydroxyl radical scavenger (EtOH and DMSO). Since copper complexes are well known to participate in DNA cleavage reaction by generation molecular oxygen or superoxide anion radical, it was observed that the addition of NaN_3 and SOD (Fig. 12 a & b, lane 4 & 5) to complexes **1** and **2** determined significant cleavage inhibition behaviour.

Furthermore, a marked inhibition of the cleavage activity of 1 and 2 was also observed in the presence of EtOH and DMSO, suggesting that diffusible hydroxyl radicals (•OH) were also involved in the cleavage reaction mechanism (Fig. 12 a & b, lane 6 & 7). The corroborative observations suggested that the these complexes were able to induce an oxidative cleavage of the plasmid DNA by generating reactive oxygen species ($^1O_2$ and $O_2^{\bullet-}$) and hydroxyl radicals (•OH) resulting in the formation of copper-oxo species [54,55].

To investigate the complexes' preferential groove binding mode, cleavage activity was measured with the addition of minor groove binding agent, DAPI (4′,6–diamidino–2–phenylindole). The electrophoretic bands (Fig. 13 a & b, lane 8) demonstrated that the addition of DAPI resulted in considerable cleavage inhibition activity resulted in the minor groove preference of **1** and **2**. These findings are of considerable interest as most of the oxidative cleaving reagents interact preferentially through minor grooves rather than major grooves [56].

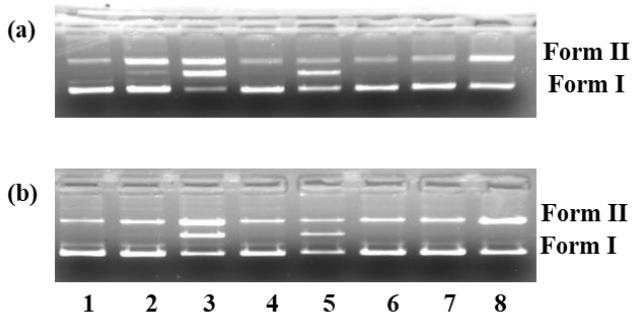

Fig. 13. cleavage behavior of pBR322 DNA (0.1 μg/μL) in the prescence of 1 and 2 at 37 °C with an incubation time of 1 h with the addition of different additives: (a) lane 1, DNA; lane 2, DNA + **1**; lane 3, H_2O_2 (0.25 μM) + DNA + **1**; lane 4, sodium azide (0.4 μM) + DNA + **1**; lane 5, SOD (0.4 μM) + DNA **+ 1**; lane 6, Ethyl alcohol (0.4 μM) + DNA + **1**; lane 7, DMSO (0.4 μM) + DNA + **1**; lane 8, DAPI (0.16 μM) + DNA + **1**; (b) lane 1, DNA; lane 2, DNA + **2**; lane 3, H_2O_2 (0.25 μM) + DNA + **2**; lane 4, sodium azide (0.4 μM) + DNA + **2**; lane 5, SOD (0.4 μM) + DNA **+ 2**; lane 6, Ethyl alcohol (0.4 μM) + DNA + **2**; lane 7, DMSO (0.4 μM) + DNA + **2**; lane 8, DAPI (0.16 μM) + DNA + **2**.

3.9.6 RNA Cleavage studies

The RNA molecule was involved in various cellular processes and performed regulatory functions, thus could be exploited as a viable therapeutic target. The metal-based complexes were found to promote specific degradation of the RNA molecule through hydrolysis of the phosphate backbone or as a sequence–recognizing moieties. Thus, investigating the RNA cleavage pathway in the presence of metal complexes could be envisaged for controlling RNA structural features and developing metallonucleases that could selectively hydrolyze RNA at the target site.

The RNA cleavage activity was monitored at a fixed concentration of tRNA which was incubated with an increasing concentration of the complexes **1** and **2** at room temperature for a period of 3 h and 24 h. After 3 hours of incubation, the complexes caused a partial cleavage of the tRNA molecule and showed moderately decreased bands, according to the gel electrophoretic pattern (Fig. 14 a & b). However, with concentration range from 6.25 μM to 17.50 μM, the cleavage activity was increased and found to be higher in complex **2** than **1**. The cleavage activity was also monitored after 24 h of incubation which revealed the occurrence of largely diminished electrophoretic bands suggesting complete degradation (90-95%) of the tRNA (Fig. 14 c & d). Furthermore, with increasing concentration, the complexes demonstrated higher activity implicated by the diminishing band intensity, which was higher in complex **2**. These findings showed that RNA cleavage was time- and concentration-dependently promoted by complexes **1** and **2** [57].

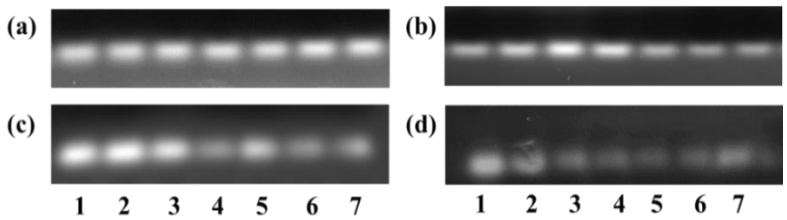

Fig. 14. The gel electrophoresis pattern of tRNA molecule with the addition of increasing concentration of complexes **1** and **2** (6.25–17.50 μM) for 3h (a and b) and for 24h (c and d).

3.10 Lipophilicity

Lipophilicity is used to determine various biological parameters of the complexes, such as cellular uptake, metabolism, bioavailability, and lipid solubility. The study has gained importance as it is ideal for predetermining the ADMET properties of drug candidate correlate structure and lipophilicity profiles, thus, rendering them a safe throughput in clinical trials. The lipophilicity can be calculated in terms of Log P, demonstrating the membrane permeability of the complexes. The SwissADME software calculated Log P values of complexes **1** and **2** as 1.28 and 2.82, respectively. The greater lipophilic nature of complex **2** than complex **1** was reflected by their LogP value, followed by their enhanced biological activity [58].

3.11 Cytotoxic profile

The cytotoxicity of both the complexes was assessed using MTT assay against three cancer cell lines *viz*., MDA-MB-231 (triple negative breast cancer cell line), HCT 116 (human colon cancer cell line) and A549 (lung cancer cell) (Fig. 15). When **1** and **2** were treated at a dosage of 10-200 µg/ml, it was found that the complexes effectively inhibited the growth of these malignant strains in a dose-dependent manner. The complex **2** observed greater inhibitory response as quantified by the calculated IC_{50} values (Table 3). This is caused due to its unsaturated and planar geometric preference that facilitates the insertion of **2** into the plasma membrane. The complex displayed a stronger inhibitory response on the tested MDA-MB-231 cancer cell line as a result of the positive association between DNA/RNA interaction and cytotoxicity. Furthermore, ROS species produced by the complexes may be responsible for inducing apoptosis in cancer cells by producing H_2O_2 levels above the toxic threshold. *In vitro* tumour cell growth is directly and dose-dependently inhibited when anticancer drugs are combined with ROS species. The morphological alterations detected in the cell lines exposed to complexes for 48 h are presented in Fig. 16 indicating that with the exposure of complexes to the cell lines, complexes **1** and **2**

presented round features and were nonadherent in culture as compared to control. These morphological changes indicated that these complexes are capable of inducing cell death, probably by apoptosis cells. However, changes in complex **2** were more pronounced as compared to complex **1**, making it as a potential cytotoxic agent.

Table 3

Complexes	**IC_{50} values (µg/ml)**		
	MDA-MB-231	**HCT-116**	**A549**
1	118.5	81.97	77.61
2	22.96	51.59	53.53

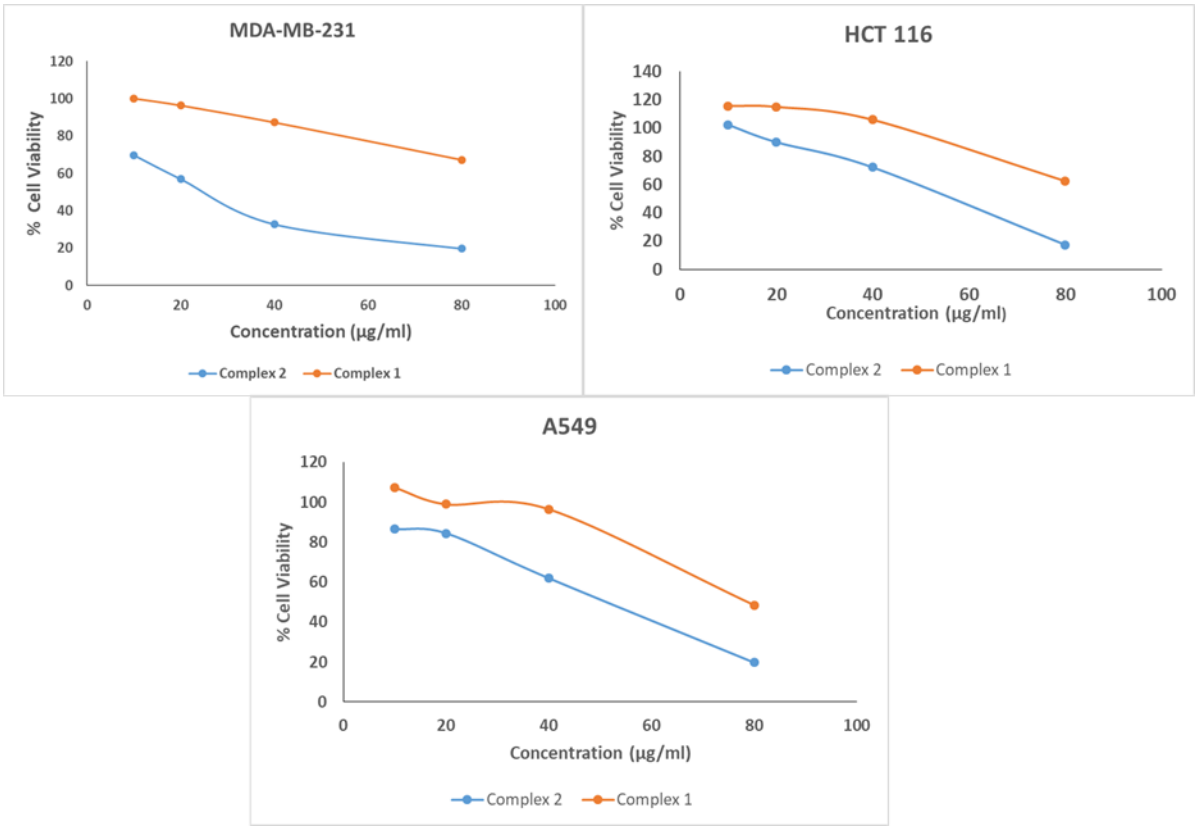

Fig. 15 Cell viability of treated cancer cells at different complexes concentrations under dark and visible conditions.

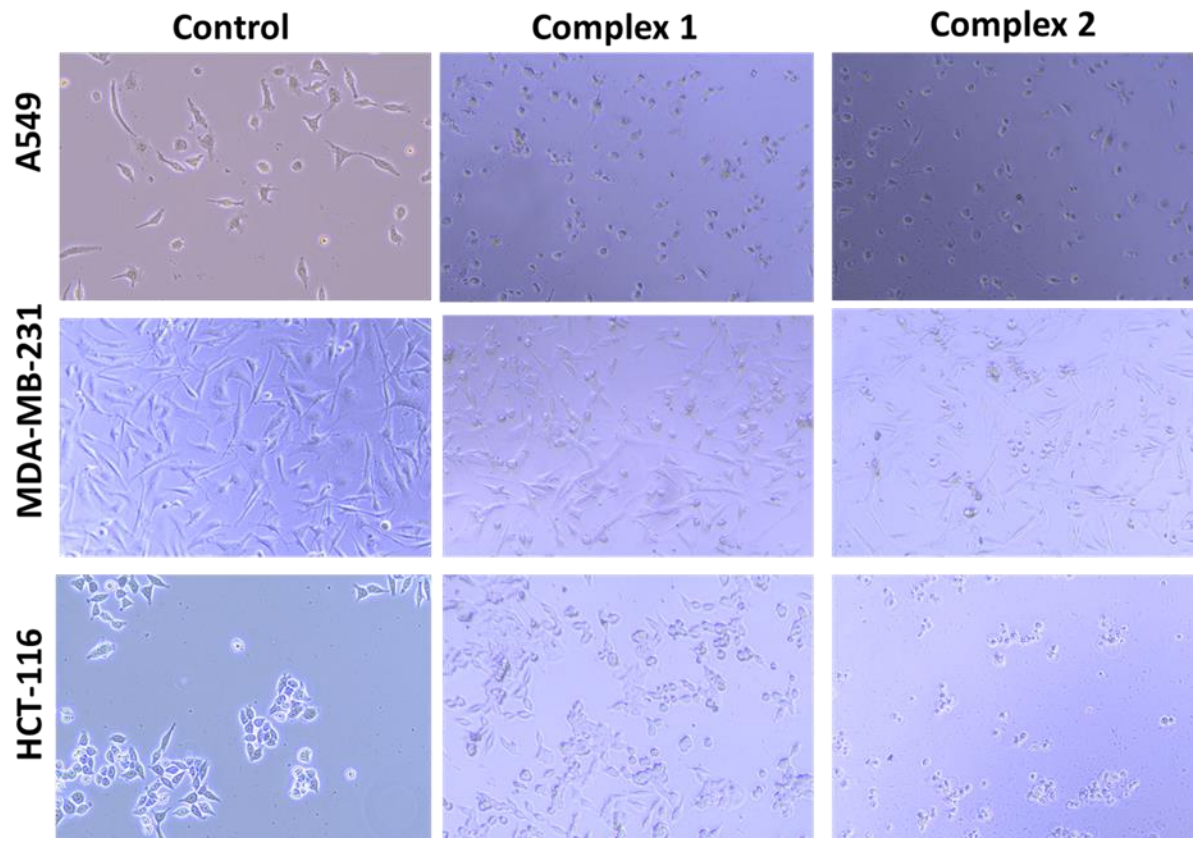

Fig. 16 The morphological alterations in different cancer cells upon treatment with complexes at their IC_{50} values (µg/ml)

3.12 Molecular docking studies

Molecular docking studies with DNA and RNA biomolecule were conducted to further confirm the binding mode as well as selective recognition sites for **1** and **2**, were carried out [59]. The docked pose model of **1** and **2** with DNA (PDB ID: 1BNA) delineated that the complexes preferentially target the minor groove GC region in proximity to G–24, C–23, G–22, G–4, G–4, A–5 and A–6 nucleobase pairs (Fig. S7 & S8a). The Schiff base ligand in the complexes was found to intercalate within the DNA nucleobases, while the imidazole moiety interacted through hydrogen bonding interactions stabilizing the overall molecular interactions. The binding energies were found to be –248 $KJmol^{-1}$ and –270 $KJ\ mol^{-1}$ for complexes **1** and **2**, respectively, suggesting the higher binding propensity of complex $[C_{16}H_{15}CuN_3O_4S]$ with DNA duplex.

The Docking profile of the complexes **1** and **2** with tRNA (PDB ID: 6tRNA) demonstrated that these complexes fit snugly into the RNA intercalation site i.e., inserted into the active pocket of the anticodon arm in proximity to C–28, C–27, A–29, G–26, C–25, G–30, C–40, G–42, G–43 and U–41 (Figure S7 & S8b). In addition, van der Waals and hydrophobic interactions also play a major role in the stronger binding of the complexes with tRNA. The binding energies for complexes **1** and **2** were found to be –265 $KJmol^{-1}$ and –299 $KJmol^{-1}$, respectively, which validates the higher binding propensity of complex **2**. Furthermore, the higher negative binding energy values of the complexes with tRNA as compared to ct–DNA demonstrated that they were better targeted towards tRNA therapeutic biomolecule.

4. Conclusions

New water soluble polymeric (μ–oxo) bridged Cu(II) complexes derived from taurine Schiff base and appended with imidazole ligand were synthesized. The structures of complexes were established by various spectroscopic and single X–ray crystallographic studies. The complex **1** crystallizes in the trigonal crystal system with the R–3 space group and complex **2** crystallizes in a monoclinic crystal system with the P 21/n space group. The crystal structure of the complexes was further stabilized by the intermolecular C----C and H----H bonding interactions resulting in a two dimensional supramolecular framework.

The DFT studies were carried out to determine the frontier molecular orbitals and other geometrical parameters of the complexes and to correlate their energy and stability. The results of DFT studies demonstrated higher stability of complex **2** as compared to **1**.

The binding profile of complexes **1** and **2** was evaluated by employing various biophysical methods *viz*., absorption titrations, fluorescence intercalator displacement assay, circular dichroism spectroscopy, and electron paramagnetic resonance binding studies with ct–

DNA/tRNA. The corroborative results of these experiments revealed that the complexes interacted via an intercalative mode with higher binding propensity of complex **2** as compared to **1**. Furthermore, the complexes show higher binding propensity towards tRNA as compared to ct–DNA implicating their selective preferential binding towards RNA. The gel electrophoretic experiments of complexes **1** and **2** were carried out with plasmid pBR322 DNA which demonstrated that the complexes were able to cleave the plasmid DNA in a dose dependent manner at low micromolar concentrations. The mechanistic insight of DNA cleavage in presence of ROS radical scavengers showed that DNA scission was facilitated suggesting the involvement of singlet oxygen ($^1O_2$) and superoxide anions ($O_2^{\bullet-}$). The cleavage studies in presence of H_2O_2 implicated a lethal double–strand DNA scission via the oxidative pathway involving the formation of copper–oxo species mediated through Fenton's reaction mechanism. The tRNA cleavage experiments of the complexes **1** and **2** were performed which revealed efficient cleavage activity of the complexes as a function of both increasing concentration and time. Molecular docking studies were also performed with DNA and RNA biomolecules which revealed higher negative binding energy values of the complexes with tRNA, validating the results obtained from spectroscopic studies.

Authorship contribution statement

Siffeen Zehra: Data curation, Investigation, Methodology, Software, Validation, Visualization, Writing-original draft. **Huzaifa Yasir Khan**: Validation, Writing-review & editing. **Thierry Roisnel**: Methodology. **Sartaj Tabassum**: Investigation. **Farukh Arjmand**: Formal analysis, Investigation, Supervision, Validation, Writing-review & editing

Acknowledgements

The SAIF Panjab University, Chandigarh is gratefully acknowledged for providing elemental analysis and ESI-MS Facilities. We are also thankful to the Department of Chemistry, Aligarh

Muslim University, for providing the spectroscopic facilities. The authors (S.Z.) sincerely acknowledge the University Grant Commission (UGC), CSIR-HRDG (SRF Scheme-2020:09/112(0660)2020-EMR-I), New Delhi, and Department of Chemistry, AMU through UGC assisted DRS-SAP, DST-FIST, and DST PURSE Programme for providing financial assistance during the research work.

Conflict of Interest

There is no conflict of interest to declare.

References

1. (a) E.J. Anthony, E.M. Bolitho, H.E. Bridgewater, O.W.L. Carter, J.M. Donnelly, C. Imberti, E.C. Lant, F. Lermyte, R.J. Needham, M. Palau, P.J. Sadler, H. Shi, F. Wang, W. Zhang, Z. Zhang, *Chem. Sci*. 11 (2020) 12888-12917. https://doi.org/10.1039/D0SC04082G. (b) B. Rosenberg, L. VanCamp, J.E. Trosko, V.H. Mansour, *Nature*, 222 (1969) 385-386. https://doi.org/10.1038/222385a0.

2. (a) C. Santini, M. Pellei, V. Gandin, M. Porchia, F. Tisato, C. Marzano, *Chem. Rev*. 114 (2014) 815-62. https://doi.org/10.1021/cr400135x. (b) C. Marzano, M. Pellei, F. Tisato, C. Santini, *Anti-Cancer Agents Med. Chem*. 9 (2009) 185-211. https://doi.org/10.2174/187152009787313837.

3. C.R. Munteanu, K. Suntharalingam, *Dalton Trans*. 44 (2015) 13796–13808. https://doi.org/10.1039/C5DT02101D. Special Edition: Metal Anticancer Compounds. *Dalton Trans* (2009) 10629−10936. https://doi.org/10.1039/B924211M.

4. K.D. Mjos, C. Orvig, *Chem. Rev*. 114 (2014) 4540−4563. https://doi.org/10.1021/cr400460s.

5. Z. Zhang, L. Zhou, N. Xie, E. C. Nice, T. Zhang, Y. Cui, C. Huang, *Signal Transduct. Target. Ther*. 5 (2020) 1-25. https://doi.org/10.1038/s41392-020-00213-8.

6. T.C. Johnstone, K. Suntharalingam, S. J. Lippard, *Chem. Rev*. 116 (2016) 3436–3486. https://doi.org/10.1021/acs.chemrev.5b00597.

7. X. Liang, D. Li, S. Leng, X. Zhu, *Biomed. Pharmacother*. 125 (2020) 109997. https://doi.org/10.1016/j.biopha.2020.109997.

8. D. Suna, W.Gao, H. Hu, S. Zhou, *Acta Pharm. Sin. B,* 12 (2022) 3049-3062. https://doi.org/10.1016/j.apsb.2022.02.002.

9. D. Bumcrot, M. Manoharan, V. Koteliansky, D.W.Y. Sah, *Nat. Chem. Biol.* 2 (2006) 711–719. https://doi.org/10.1038/nchembio839.

10. M. Matsui, D. Corey, *Nat. Rev. Drug Discov*. 16 (2017) 167–179. https://doi.org/10.1038/nrd.2016.117.

11. S. Zehra, T. Roisnel, F. Arjmand, *ACS Omega*, 4 (2019) 7691–7705. https://doi.org/10.1021/acsomega.9b00131.

12. V.J. DeRose, M.V. Yglesias, 8.39 - Metal Ion Interactions With DNA, RNA, and Nucleic Acid Enzymes, in E.C. Constable, G. Parkin, L.Q. Jr (Eds.) Comprehensive Coordination Chemistry III, 2021, pp. 968-993. https://doi.org/10.1016/B978-0-08-102688-5.00112-4.

13. F. Arjmand, Z. Afsan, S. Sharma, S. Parveen, I. Yousuf, S. Sartaj, H.R. Siddique, S. Tabassum, *Coord. Chem. Rev*. 387 (2019) 47-59. https://doi.org/10.1016/j.ccr.2019.02.015.

14. K.L. Haas, K.J. Franz, *Chem. Rev.* 109 (2009) 4921–4960. https://doi.org/10.1021/cr900134a.

15. A. Kellett, Z. Molphy, C. Slator, V. McKee, N.P. Farrell, *Chem. Soc. Rev*. 48 (2019) 971—988. https://doi.org/10.1039/C8CS00157J.

16. H.Y. Khan, M.O. Ansari, G.G.H.A. Shadab, S. Tabassum, F. Arjmand, *Bioorg. Chem*. 88 (2019) 102963. https://doi.org/10.1016/j.bioorg.2019.102963.

17. (a) H.Y. Khan, S.K. Maurya, H.R. Siddique, S. Yousuf, F. Arjmand, *ACS omega, 5* (2020) 15218-15228. https://doi.org/10.1021/acsomega.0c01206. (b) C.S. Chow, F.M. Bogdan, *Chem. Rev*. 97 (1997) 1489−1514. https://doi.org/10.1021/cr960415w.

18. F. Wang, P. Jiao, M. Qi, M. Frezza, Q. P. Dou, B. Yan, *Curr. Med. Chem*. 17 (2010) 2685–2698. https://doi.org/10.2174/092986710791859315.

19. M. Wehbe, A.W. Leung, M.J. Abrams, C. Orvig, M.B. Bally, *Dalton Trans.* 46 (2017) 10758-10773. https://doi.org/10.1039/C7DT01955F.

20. J. Hu, F. Piao, S.W. Schaffer, A. El Idrissi, J.Y. Wu, Taurine 11, Springer, 2019.

21. S. Schaffer, H.W. Kim, *Biomol. Ther.* 26 (2018) 225–241. https://doi.org/10.4062%2Fbiomolther.2017.251

22. X. Zhang, S. Tu, Y. Wang, B. Xu, F. Wan, *Acta Biochim. Biophys. Sin*. 46 (2014) 261–272. https://doi.org/10.1093/abbs/gmu004.

23. I.M. El Agouza, S.S. Eissa, M.M. El Houseini, D.E. El–Nashar, O.M. Abd El Hameed, *Angiogenesis*, 14 (2011) 321–330. https://doi.org/10.1007/s10456-011-9215-3.

24. S. Srivastava, R. Roy, S. Singh, P. Kumar, D. Dalela, S. N. Sankhwar, A. Goel, A.A. Sonkar, *Cancer Biomark*. 6 (2010) 11–20. https://doi.org/10.3233/CBM-2009-0115.

25. R.H. Morales-Borge, M.J. González, R.C. Gupta, O. Ayeotan, *Cancer Case Reports*, 1 (2020) 1-14. http://dx.doi.org/10.47733/GJCCR.2020.1205.

26. M. Li, L.L. Kong, Y. Gou, F. Yang, H. Liang, *Spectrochim. Acta – Part A Mol. Biomol. Spectrosc*. 128 (2014) 686–693. https://doi.org/10.1016/j.saa.2014.02.197.

27. S.W. Schaffer, C.J. Jong, T. Ito, J. Azuma, *Amino Acids*, 46 (2014) 47-56. https://doi.org/10.1007/s00726-012-1414-8.

28. F. Tisato, C. Marzano, M. Porchia, M. Pellei, C. Santini, *Med. Res. Rev*. 30 (2010) 708–749. https://doi.org/10.1002/med.20174.

29. (a) C. Duncan, A.R. White**,** *Metallomics*, 4 (2012) 127–138. https://doi.org/10.1039/c2mt00174h, (b) C.L. Liu, J.Y. Zhou, Q.X. Li, L.J. Wang, Z.R. Liao, H.B. Xu, *J. Inorg. Biochem*., 75 (1999) 233–240. https://doi.org/10.1016/S0162-0134(99)00037-9.

30. (a) S. Tardito, L. Marchiò, Curr. Med. Chem. 16 (2009) 1325-1348. https://doi.org/10.2174/092986709787846532. (b) A. Gupte, R.J. Mumper, *Cancer Treat. Rev*. 35 (2009) 32–46. https://doi.org/10.1016/j.ctrv.2008.07.004.

31. R. Galindo-Murillo, J.C. Garcia-Ramos, L. Ruiz-Azuara, T.E. Cheatham III, F. Cortes-Guzman, *Nucleic Acids.Res.*, 43 (2015) 5364–5376. https://doi.org/10.1093/nar/gkv467.

32. T.L. Yusuf, S.D. Oladipo, S. Zamisa, H.M. Kumalo, I.A. Lawal, M.M. Lawal, N. Mabuba, *ACS omega*, 6 (2021) 13704-13718. https://doi.org/10.1021/acsomega.1c00906.

33. S. Zehra, S. Tabassum, F. Arjmand, *Drug Discovery Today*, 26 (2021) 1086-1096. https://doi.org/10.1016/j.drudis.2021.01.015.

34. C.L. Liu, J.Y. Zhou, Q.X. Li, L.J. Wang, Z.R. Liao, H. B. Xu, *J. Inorg. Biochem.* 75 (1999) 233–240. https://doi.org/10.1016/S0162-0134(99)00037-9.

35. S. Zehra, I. Cirilli, S. Silvestri, S. Gómez-Ruiz, S. Tabassum, F. Arjmand, *Metallomics*, 13 (2021) mfab064. https://doi.org/10.1093/mtomcs/mfab064.

36. S. Khursheed, S. Tabassum, F. Arjmand, *Polyhedron*, 214 (2022) 115638. https://doi.org/10.1016/j.poly.2021.115638.

37. R. Grimmett, A.R. Katritzky, A.J. Boulton, Advances in Heterocyclic Chemistry, vol. 27, Academic Press; New York, 1980.

38. A.K. Gopalakrishnan, S.A. Angamaly, M.P. Velayudhan, 6 (2021) 10918-10947. https://doi.org/10.1002/slct.202102619.

39. H.Y. Khan, M.T. Zeyad, S. Akhter, S. Tabassum, F. Arjmand, *Inorg. Chim. Acta*, 538 (2022) 120978. https://doi.org/10.1016/j.ica.2022.120978.

40. M. Li, Y. Gou, F. Yang, H. Liang, *Spectrochim. Acta– Part A Mol. Biomol. Spectrosc.* 128 **(**2014) 686–693. https://doi.org/10.1016/j.saa.2014.02.197.

41. S. Muthuramalingam, S. Subramaniyan, T. Khamrang, M. Velusamy, R. Mayilmurugan, *ChemistrySelect*, 2 (2017) 940-948. https://doi.org/10.1002/slct.201601786.

42. A. Shirvan, H. Golchoubian, E. Bouwman, *J. Mol. Struct*. 1195 **(**2019) 769–777. https://doi.org/10.1016/j.molstruc.2019.06.034.

43. L.–Q. Chai, L. Zhou, H.–B. Zhang, K.–H. Mao, H.–S. Zhang, *New J. Chem*. 43 **(**2019) 12417–12430. https://doi.org/10.1039/C9NJ01920K.

44. P. Manna, S.K. Seth, A. Das, J. Hemming, R. Prendergast, M. Helliwell, S.R. Choudhury, A. Frontera, S. Mukhopadhyay, *Inorg. Chem*. 51 **(**2012) 3557–3571. https://doi.org/10.1021/ic202317f.

45. J. Liu, T. Zhang, T. Lu, L. Qu, H. Zhou, Q. Zhang, L. Ji, *J. Inorg. Biochem*. 91 **(**2002) 269–276. https://doi.org/10.1016/S0162-0134(02)00441-5.

46. D. S. Raja, N. S. P. Bhuvanesh and K. Natarajan, *Eur. J. Med. Chem*. 46 **(**2011) 4584–4594. https://doi.org/10.1016/j.ejmech.2011.07.038.

47. A. Wolfe, G.H. Shimer Jr, T. Meehan, *Biochemistry*, 26 (1987) 6392–6396. https://doi.org/10.1021/bi00394a013.

48. S. Manna, E. Zangrando, H. Puschmann, S.C. Manna, *Polyhedron*, 162 **(**2019) 285–292. https://doi.org/10.1016/j.poly.2019.01.057.

49. A. Jayamani, R. Bellam, G. Gopu, S.O. Ojwach, N. Sengottuvelan, *Polyhedron*, 156 **(**2018) 138–149. https://doi.org/10.1016/j.poly.2018.09.011.

50. H.Y. Khan, S. Tabassum, F. Arjmand, *RSC Advances*, 10 **(**2020) 166-178. https://doi.org/10.1039/C9RA07464C.

51. B. Lippert, Coordinative bond formation between metal ions and nucleic acid bases, in: Nucleic Acid–Metal Ion Interact. Royal Society of Chemistry: Cambridge, United Kingdom, 2008, 39–74.

52. G. Facchin, E. Kremer, D.A. Barrio, S. B. Etcheverry, A.J. Costa–Filho, M.H. Torre, *Polyhedron*, 28 **(**2009) 2329–2334. https://doi.org/10.1016/j.poly.2009.04.029.

53. S. Sharma, L. Toupet, F. Arjmand, *New J. Chem*. 41 (2017) 2883-2886. https://doi.org/10.1039/C7NJ00563F.

54. A. Jayamani, N. Sengottuvelan, S.K. Kang, Y.–I. Kim, *Polyhedron*, 98 **(**2015) 203–216. https://doi.org/10.1016/j.poly.2015.05.042.

55. X. Qiao, Z.–Y. Ma, C.–Z. Xie, F. Xue, Y.–W. Zhang, J.–Y. Xu, Z.–Y. Qiang, J.–S. Lou, G. –J. Chen, S.–P. Yan, *J. Inorg. Biochem*. 105 **(**2011) 728–737. https://doi.org/10.1016/j.jinorgbio.2011.01.004

56. H.Y. Khan, S. Zehra, S. Parveen, I. Yousuf, S. Tabassum, F. Arjmand, *ChemistrySelect*, 3 (2018) 12764-12772. https://doi.org/10.1002/slct.201802698.

57. F. Arjmand, I. Yousuf, T. Ben Hadda, L. Toupet, *Eur. J. Med. Chem.* 81 **(**2014) 76–88. https://doi.org/10.1016/j.ejmech.2014.04.080.

58. C. Zhang, M.–L. Maddelein, R.W.–Y. Sun, H. Gornitzka, O. Cuvillier, C. Hemmert, *Eur. J. Med. Chem.* 157 **(**2018) 320– 332. https://doi.org/10.1016/j.ejmech.2018.07.070.

59. P. Roozbahani, M. Salehi, R. E. Malekshah and M. Kubicki, *Inorg. Chim. Acta*, **496 (**2019) 119022. https://doi.org/10.1016/j.ica.2019.119022.